Molecular Physics, Vol. 103, No. 2–3, 20 January–10 February 2005, 229–248

Taylor & Francis
Taylor & Francis Group

Two-photon vibronic spectroscopy of allene at 7.0–10.5 eV: experiment and theory

JAU-CHIN SHIEH[†], JEN-CHIEH WU[†], RUNHUA LI[‡], JIA-LIN CHANG[‡§], YI-JI LIN[‡]**, DAI-WEI LIAO[‡]**, M. HAYASHI[¶], A. M. MEBEL[‡|], NICHOLAS C. HANDY[‖] and YIT-TSONG CHEN[†‡]*

[†]Department of Chemistry, National Taiwan University, Taipei 106, Taiwan
[‡]Institute of Atomic and Molecular Sciences, Academia Sinica, P.O. Box 23-166, Taipei 106, Taiwan
[§]Department of Science Education, National Taichung Teachers College, Taichung 403, Taiwan
[¶]Center for Condensed Matter Sciences, National Taiwan University, Taipei 106, Taiwan
[|]Department of Chemistry and Biochemistry, Florida International University, Miami, Florida 33199, USA
[‖]Department of Chemistry, University of Cambridge, Cambridge, CB2 1EW, UK

(*Received 15 July 2004, accepted 19 August 2004*)

2 + 1 resonance-enhanced multiphoton ionization (REMPI) spectra of allene at 7.0–10.5 eV have been observed. The excited vibronic symmetry has been determined from polarization-ratio measurements. Based on the vibronic energies and peak intensities calculated using *ab initio* MO and time-dependent density functional theory, the very congested REMPI spectra have been assigned as due to $\pi^* \leftarrow \pi$, $3p \leftarrow \pi$, $4s \leftarrow \pi$, $4p \leftarrow \pi$, and $4d \leftarrow \pi$ transitions. Vibrational progressions related to the CH_2 twisting ($\nu_4 \sim 770\,cm^{-1}$) have been observed for several excited electronic states. Calculated Franck–Condon factors also confirm that CH_2 twisting is the most active mode in the vibronic spectra of allene. In this study, theoretical calculations of two-photon intensities and polarization ratios have been made through the *ab initio* computed one-photon transition dipole moments to various electronic states as intermediates. As a starting point to interpret the complicated vibronic spectrum of allene, the theoretical approach, without vibronic couplings, has been applied to predict the peak positions, spectral intensities, and polarization ratios of Rydberg states, and qualitatively shows a considerable agreement with experimental observations.

1. Introduction

The photolysis of allene (CH_2CCH_2) at 193 nm shows that the dissociation pathways in the primary process involve H and H_2 eliminations [1, 2]. Theoretical studies have proposed that the allene molecule, in the photolysis at 193 nm, undergoes internal conversion to its ground state surface prior to dissociation [3, 4]. Recently, speculation about possible isomerization between allene and its geometric isomer of propyne (CH_3CCH) during photodissociation has attracted many investigations [2, 3, 5, 6]. The mechanisms for the isomerization of allene and propyne involve H atom migration and ring closure. Many isomeric intermediates on the C_3H_4 potential energy surface, such as cyclopropene, propenylidene, vinylmethylene etc., and the final photofragments, e.g. C_3H_3 and C_3H_2, play important roles in organic chemistry [7–10]. The photodissociation of allene not only serves as a prototypical model for the study of intramolecular rearrangements, but also provides a fundamental basis for the reactions of hydrocarbons.

Allene is the most fundamental molecule among the cumulene compounds and is the simplest example of a diolefin system. Structural studies of allene by electronic spectroscopy have been performed using low-resolution one-photon absorption [11–14], electron impact [15], and magnetic circular dichroism methods [16, 17]. The vibronic spectrum of allene is of extraordinary

* Corresponding author. Email: ytchen@pub.iams.sinica.edu.tw
** On leave from Institute of Physical Chemistry, Department of Chemistry and State Key Lab of Physical Chemistry on Solid Surfaces, Xiamen University, Xiamen, Fujian 361005, China.

Molecular Physics
ISSN 0026–8976 print/ISSN 1362–3028 online © 2005
Taylor & Francis Group Ltd
http://www.tandf.co.uk/journals
DOI: 10.1080/00268970512331317354

complexity, because of the dramatic geometry change from the D_{2d} ground state to excited states, with the HCCH dihedral angles being much less than 90°. This case is similar to ethylene, in which the unusually outspreading Franck–Condon factors of the $\pi^* \leftarrow \pi$ transition (from D_{2h} to D_{2d}) make the vibronic bands extend from 58 000 to 85 000 cm^{-1} [18, 19].

Despite their importance for understanding the photodissociation mechanisms, the potential energy surfaces of allene have so far heavily relied on theoretical calculations [3, 4] without sufficient spectroscopic examination. Following the photodissociation studies of propyne and allene at 193 nm in our laboratory [6, 20], we investigated the excited vibronic states of these two molecules at 6.8−10.5 eV using $2+1$ resonance-enhanced multiphoton ionization (REMPI) spectroscopy. The two-photon resonance ionization spectrum of propyne has already been published [21]. In this article, we discuss the observed REMPI spectra of allene at 7.0–10.5 eV corresponding to the vibronic transitions of $\pi^* \leftarrow \pi$, $3p \leftarrow \pi$, $3d \leftarrow \pi$, $4s \leftarrow \pi$, $4p \leftarrow \pi$, and $4d \leftarrow \pi$, involving valence and Rydberg excited electronic states.

As discussed for propyne [21], compared with one-photon absorption spectroscopy, the advantages of applying a REMPI laser technique to study the high-lying excited electronic states (≥6 eV) of polyatomic molecules are as follows. First, the spectral resolution of tunable dye lasers is usually better than that of conventional VUV light source. Detailed molecular structures can be resolved. Second, REMPI spectroscopy can judiciously single out stable excited states leading to a simplified spectrum. Excited states with fast (pre)dissociation rate, compared to the ionization rate during a multiphoton process, can be excluded from REMPI spectrum unless very high laser power is used. Third, the totally symmetric vibronic excited states can be unambiguously identified from measuring their polarization-ratios, $\Omega = I_{circular}/I_{linear}$, by REMPI spectroscopy [21–23]. Fourth, combining with time-of-flight (TOF) mass spectrometry, signal corresponding to a particular mass of interest can be discriminated from other species.

As will be seen in the following sections, the $2+1$ REMPI spectra of allene are very congested. The vibronic transitions to an excited electronic state are not distinctively isolated from those to other electronic states. As such, traditional spectral analysis in light of the regularity of vibrational progressions is unlikely applicable. In this study, experimental results are compared with theoretical vertical excitation energies for the $\pi^* \leftarrow \pi$ valence and $ns \leftarrow \pi$, $np \leftarrow \pi$, and $nd \leftarrow \pi$ ($n = 3, 4$) Rydberg states of allene. The theoretical excitation energies have been calculated using recently developed time-dependent density functional theory (TDDFT) and an *ab initio* MRCI method. Comparison of theory and experiment allowed us to assess the accuracy of the TDDFT approach and assisted in the spectroscopic assignment for the REMPI experimental data.

The rest of this paper is organized as follows. Section 2 describes the experimental approach. Section 3 presents density functional theory and *ab initio* molecular orbital (MO) calculations. Two-photon intensities and polarization ratios in the $2+1$ REMPI spectra of allene were also calculated. Next, section 4 provides discussions for a spectroscopic attempt to assign the observed vibronic transitions of allene. Finally, conclusions are addressed in section 5.

2. Experiment

The REMPI experiment on allene was performed using a TOF mass spectrometer, as described in the studies of propyne [21], vinyl chloride [24, 25], allyl radical [26, 27], and 2-methylallyl radical [28]. Briefly, allene was purchased from Fluka and mixed with 2 atm He to form a 10% mixture. Adiabatic expansion through a pulsed valve (General Valve, 0.5 mm orifice) cools the seeded molecules of allene. The expanded molecular beam (180 μs duration) was skimmed and injected into the TOF tube. A tunable dye laser (Lambda Physik, Scanmate 2E) pumped by a Nd:YAG laser (Spectra Physics, GCR-190) was scanned to cover the spectral range 58 000–82 000 cm^{-1}. The spectral resolution of the grating scan was ~0.2 cm^{-1}. The laser beam was tightly focused by a lens and aligned to intersect the molecular beam. The allene cations produced via REMPI were repelled in an electric field with direction perpendicular to both laser and molecular beams. These ions flew across the field-free TOF tube (80 cm) and were detected by a microsphere plate (MSP, E1-Mu1). The time-sequence of the laser and molecular beams in this experiment was controlled by a digital pulse/delay generator (Stanford Research System, DG535).

The detected TOF signal from the MSP was amplified by a preamplifier (EG&G, VT120) and sent to a digital oscilloscope (LeCroy, 9344) and personal computer. In the REMPI experiment, the amplified signal was processed in a gated integrator (Stanford Research System, SR250) and then an A/D converter. A computer program was developed to control the dye laser and to acquire the digitized data from the A/D converter. The REMPI spectra were obtained by gating at a selected mass, and monitoring the ion yield as a function of excitation laser wavelength. For each step in the wavelength scan, signal was averaged for 60–100 laser

shots to reduce the noise caused by laser fluctuation. An optogalvanic hollow-cathode lamp filled with Ne (Hamamatsu, L233-13NB) was employed simultaneously in the spectral scan for wavelength calibration. In this experiment, the $C_3H_3^+$ ($m/z = 39$) channel was used to obtain the REMPI spectra as it typically gave stronger signals than the parent ion of $C_3H_4^+$ ($m/z = 40$); the spectra obtained from these two channels were proved, with much care, to be the same within experimental uncertainty. In the case when the parent-ion signal was too weak, a photon counter (Stanford Research System, SR400) was used to replace the gated integrator.

The polarization ratio for a particular transition was measured taking the TOF intensity of the $C_3H_3^+$ signal with laser wavelength fixed at the top of the transition. The integrated intensity was measured with linearly and circularly polarized lasers separately, and was averaged for 1000 laser shots for each measurement. As such, the energy fluctuation of the two polarized lasers can be reduced within 0.5%. Further details of the alignment for the polarization-ratio measurements can be found in reports on the propyne study [21].

3. Calculations

3.1. *Density functional calculations*

The time-dependent density functional theory is a powerful method for the prediction of excitation spectra. This is a response theory, excitation energies being calculated from the poles of the frequency dependent polarizability and oscillator strengths from the residues. A number of research groups have recommended this approach [29–36]. Recently, we successfully applied this method to study Rydberg excited electronic states of propyne [21].

It is necessary to amend a straightforward implementation of time dependent theory in order to obtain Rydberg excited states [31, 33]. Handy and coworkers [31] found it simplest to 'graft' a correction to the exchange-correlation potential, in the molecular asymptotic region. This correction is $-1/r + IE + \varepsilon_{\text{homo}}$, where IE is the ionization energy, r is the distance of the point from the molecule and $\varepsilon_{\text{homo}}$ is the Kohn–Sham homo eigenvalue, as computed using a generalised gradient approximation (GGA) functional. In these studies we use grafting parameters (3.0, 4.0) to describe the connection region. Full details may be found in [31].

In these studies we used Handy's GGA functional HCTH [29], whose parameters have been refined through least squares to the properties of a 93 molecule 'fitting' set. Kohn–Sham calculations are performed with this functional, and then the orbitals and orbital energies are used, in conjunction with appropriate derivatives of HCTH, to construct the electric and magnetic hessians, h_1, h_2, from which the excitation energies are determined through an eigenproblem. Our experience using this functional suggests that it is reasonable to expect the mean absolute accuracy of the calculated excitation energies to be around 0.2 eV [30, 31].

The calculations were performed on allene using CADPAC [37]. The contracted basis set used can be described by H (3s2p), C (5s4p2d), together with diffuse s (0.01, 0.04), p (0.01, 0.04, 0.0025) and d (0.01, 0.04, 0.0025) Gaussians at the centre of the molecule. High accuracy quadrature was used. The resulting excitation energies and oscillator strengths are given in table 1. The symmetry of the electronic excited state is immediately available; the description of these singly excited singlet states is obtained from the leading coefficients of the eigenvectors.

3.2. *CASSCF and MRCI calculations*

Additionally, we carried out *ab initio* MO complete active space SCF (CASSCF) [38] and multireference configuration interaction (MRCI) [39] calculations employing the MOLPRO-98 program [40]. We used the 6-311(2+)G** basis set suggested by Wyberg *et al.* [41] for the calculations of valence and low-lying Rydberg excited states of hydrocarbons. This basis set includes the standard 6-311G** basis set with two additional sp functions on carbons with exponents of 0.0438 and 0.0131928. Since the CASSCF and MRCI calculations are much more computationally demanding than TDDFT, the basis set is smaller but it was shown to provide reliable results for low-lying excited states [41]. The active space used for CASSCF and MRCI consists of four π electrons distributed on eleven orbitals. These include π and π^* valence orbitals as well as 3s, 3p, and 3d Rydberg orbitals of carbon atoms. The calculations were performed using the D_2 subgroup of a D_{2d} symmetry group, and the degenerate ^1E states were treated as two states, $^1B_2 + {}^1B_3$. In order to compute the transition dipole moments between various electronic states used in the calculation of two-photon intensities, we carried out state-average CASSCF calculations for 22 electronic states (seven ^1A, five $^1B_1$, $^1B_2$, and $^1B_3$ each in D_2 symmetry). The calculated components of transition dipole moments between various electronic states of allene are listed in table 2.

In order to predict the vibronic spectra for transitions to the Rydberg states of allene, we performed geometry optimization of seven electronic states 2^1A_1 (3^1A in D_2), 1^1B_2 (2^1B_1), 2^1E (2^1B_3 and 2^1B_2), 2^1A_2 (3^1B_1), 2^1B_1 (4^1A),

Table 1. Calculated vertical and adiabatic energies, two-photon intensities, and Franck–Condon factors for the vibronic transitions of allene.

State			Vertical energy[a,b]		Adiabatic energy[a]	Two-photon intensity[d]		Vibronic	Franck–Condon
D_{2d}	D_2	Character	EOM-CCSD[c]	TDDFT	(MRCI)	RC[e]	ZZ[f]	peak	factor
1^1A_2	1^1B_1	(π, π^*)	6.23 (0.0)	5.84 (0.0)					
1^1B_1	2^1A	(π, π^*)	6.65 (0.0)	6.04 (0.0)					
1^1E_1	$1^1B_2 + 1^1B_3$	$(\pi, 3s)$	7.02 (0.03)	6.85 (0.04)					
2^1A_1	3^1A	(π, π^*)	7.69 (0.0)	7.09 (0.0)	7.17	4.42	2.95	0_0^0	2.01×10^{-3}
					7.27			4_0^1	1.17×10^{-2}
					7.36			4_0^2	3.39×10^{-2}
					7.46			4_0^3	6.46×10^{-2}
					7.55			4_0^4	9.08×10^{-2}
					7.65			4_0^5	1.01×10^{-1}
					7.74			4_0^6	9.20×10^{-2}
					7.84			4_0^7	7.09×10^{-2}
					7.94			4_0^8	4.72×10^{-2}
					8.03			4_0^9	2.75×10^{-2}
					8.13			4_0^{10}	1.42×10^{-2}
1^1B_2	2^1B_1	$(\pi, \pi^*)/(\pi, 3p_{x,y})$	7.62 (0.41)	7.47 (0.43)	7.18	1.21	1.81	0_0^0	1.13×10^{-2}
					7.28			4_0^1	4.95×10^{-2}
					7.37			4_0^2	1.07×10^{-1}
					7.47			4_0^3	1.52×10^{-1}
					7.56			4_0^4	1.58×10^{-1}
					7.66			4_0^5	1.30×10^{-1}
					7.75			4_0^6	8.70×10^{-2}
					7.85			4_0^7	4.91×10^{-2}
					7.94			4_0^8	2.37×10^{-2}
					7.54			1_0^1	7.40×10^{-5}
					7.64			$4_0^1 1_0^1$	3.25×10^{-4}
								$4_0^2 1_0^1$	7.04×10^{-4}
								$4_0^3 1_0^1$	9.97×10^{-4}
								$4_0^4 1_0^1$	1.04×10^{-3}
								$4_0^5 1_0^1$	8.53×10^{-4}
								$4_0^6 1_0^1$	5.72×10^{-4}
2^1E_1	2^1B_3	$(\pi, 3p_z)$	7.82 (0.02)	7.63 (0.04)	7.30	4.09	2.73	0_0^0	5.42×10^{-1}
					7.40			4_0^1	2.78×10^{-1}
					7.50			4_0^2	6.11×10^{-2}
					7.59			4_0^3	7.42×10^{-3}
					7.69			4_0^4	5.23×10^{-4}
					7.43			3_0^1	5.58×10^{-2}
	2^1B_2	$(\pi, 3p_z)$	7.82 (0.02)	7.63 (0.04)	7.66	4.55	3.04	0_0^0	1.00×10^{-2}
					7.76			4_0^1	4.41×10^{-2}
					7.86			4_0^2	9.54×10^{-2}

(*continued*)

Table 1. Continued.

State			Vertical energy[a,b]		Adiabatic energy[a]	Two-photon intensity[d]			
D_{2d}	D_2	Character	EOM-CCSD[c]	TDDFT	(MRCI)	RC[e]	ZZ[f]	Vibronic peak	Franck–Condon factor
					7.95			4_0^3	1.35×10^{-1}
					8.05			4_0^4	1.41×10^{-1}
					8.14			4_0^5	1.16×10^{-1}
					8.24			4_0^6	7.74×10^{-2}
					8.33			4_0^7	4.36×10^{-2}
					8.43			4_0^8	2.11×10^{-2}
					8.03			1_0^1	2.35×10^{-3}
					8.13			$4_0^1 1_0^1$	1.03×10^{-2}
					8.22			$4_0^2 1_0^1$	2.23×10^{-2}
					8.32			$4_0^3 1_0^1$	3.16×10^{-2}
					8.41			$4_0^4 1_0^1$	3.30×10^{-2}
					8.51			$4_0^5 1_0^1$	2.70×10^{-2}
					8.60			$4_0^6 1_0^1$	1.81×10^{-2}
2^1A_2	3^1B_1	$(\pi, 3p_{x,y})$	8.05 (0.0)	7.86 (0.0)	7.83	1.69	1.13	0_0^0	8.02×10^{-3}
					7.93			4_0^1	3.73×10^{-2}
					8.02			4_0^2	8.52×10^{-2}
					8.12			4_0^3	1.28×10^{-1}
					8.21			4_0^4	1.41×10^{-1}
					8.31			4_0^5	1.23×10^{-1}
					8.40			4_0^6	8.76×10^{-2}
					8.50			4_0^7	5.25×10^{-2}
					8.59			4_0^8	2.70×10^{-2}
2^1B_1	4^1A_1	$(\pi, 3p_{x,y})$	8.06 (0.0)	7.87 (0.0)	8.01	1.50	2.25	0_0^0	1.45×10^{-2}
					8.10			4_0^1	5.91×10^{-2}
					8.20			4_0^2	1.19×10^{-1}
					8.29			4_0^3	1.56×10^{-1}
					8.39			4_0^4	1.50×10^{-1}
					8.48			4_0^5	1.14×10^{-1}
					8.58			4_0^6	7.04×10^{-2}
					8.67			4_0^7	3.65×10^{-2}
					8.27			4_0^8	1.62×10^{-2}
3^1A_1	5^1A	$(\pi, 3p_{x,y})$	8.27 (0.0)	7.94 (0.0)	8.34	9.61	14.4	0_0^0	6.07×10^{-1}
					8.43			4_0^1	2.27×10^{-1}
					8.52			4_0^2	3.43×10^{-2}
					8.46			3_0^1	7.98×10^{-2}
					8.56			$4_0^1 3_0^1$	2.98×10^{-2}
3^1E_1	$3^1B_2 + 3^1B_3$	$(\pi, 3d_{z^2})$	8.46 (0.019)	8.33 (0.02)					
2^1B_2	4^1B_1	$(\pi, 3d_{xz,yz})/(\pi, 3p_{x,y})$	8.61	8.40 (0.27)					
4^1E_1	$4^1B_2 + 4^1B_3$	$(\pi, 3d_{x^2-y^2})$		8.46 (0.02)					
3^1B_1	6^1A_1	$(\pi, 3d_{xz,yz})$		8.53 (0.0)					

(*continued*)

Table 1. Continued.

State			Vertical energy[a,b]		Adiabatic energy[a]	Two-photon intensity[d]		Vibronic peak	Franck–Condon factor
D_{2d}	D_2	Character	EOM-CCSD[c]	TDDFT	(MRCI)	RC[e]	ZZ[f]		
3^1A_2	5^1B_1	$(\pi, 3d_{xz,yz})$		8.54 (0.0)					
5^1E_1	$5^1B_2+5^1B_3$	$(\pi, 3d_{xy})$		8.56 (0.0)					
4^1A_1	7^1A_1	$(\pi, 3d_{xz,yz})$		8.56 (0.0)					
6^1E_1	$6^1B_2+6^1B_3$	$(\pi, 4s)$		8.62 (0.0)					
3^1B_2	6^1B_1	$(\pi, 3d_{xz,yz})$		8.63 (0.23)					
7^1E_1	$7^1B_2+7^1B_3$	$(\pi, 4p_z)$		8.93 (0.0)					
4^1B_1	8^1A_1	$(\pi, 4p_{x,y})$		8.97 (0.0)					
4^1A_2	7^1B_1	$(\pi, 4p_{x,y})$		8.97 (0.0)					
5^1A_1	9^1A_1	$(\pi, 4p_{x,y})$		8.98 (0.0)					
4^1B_2	8^1B_1	$(\pi, 4p_{x,y})$		9.05 (0.08)					
8^1E_1	$8^1B_2+8^1B_3$	$(\pi, 4d_{x^2-y^2})$		9.14 (0.0)					
9^1E_1	$9^1B_2+9^1B_3$	$(\pi, 4d_z{}^2)$		9.14 (0.0)					
10^1E_{11}	$10^1B_2+10^1B_3$	$(\pi, 4d_{xy})$		9.18 (0.0)					
5^1B_1	10^1A_{11}	$(\pi, 4d_{xz,yz})$		9.20 (0.0)					
5^1A_2	9^1B_1	$(\pi, 4d_{xz,yz})$		9.20 (0.0)					

[a]Unit: eV.
[b]Values in parentheses are oscillator strengths for one-photon transitions.
[c]From [4].
[d]In arbitrary units.
[e]For circular-polarized laser light.
[f]For linear-polarized laser light.

and 3^1A_1 (5^1A). Since Rydberg state geometry is often similar to the structure of cation (D_2 symmetry for allene), we restricted the optimization to D_2 symmetry. The optimized geometries are shown in table 3. Since vibrational frequency calculations for higher electronic states are still not feasible at this time, we assumed here that vibrational frequencies of the Rydberg states are similar to those of allene cation and used the cation's frequencies in calculations of vibronic spectra. Theoretical and available experimental frequencies of allene [13] and its cation [42] are shown in table 4.

The optimized structures of excited states and vibrational frequencies of the neutral and cationic allene were used for the calculation of Franck–Condon factors for various vibronic transitions using the theoretical approach suggested by us and described earlier [18, 19, 43]. In the calculations, we took into account the displacement and distortion of harmonic oscillators corresponding to the normal modes ν_1–ν_4 of *a* symmetry in the D_2 group. The calculated EOM-CCSD/6-31(2+)G* energies, oscillator strengths, and Franck–Condon factors are also tabulated in table 1.

3.3. *Calculations of two-photon intensities and polarization ratios*

In order to compare theoretical and experimental vibronic spectra of allene, we derived theoretical formula for two-photon transition probabilities. We consider a model for the two-photon absorption process in which photons interact with a molecule in two modes λ (the polarization vector $\vec{\lambda}$ and the energy $\hbar\omega_\lambda$) and κ ($\vec{\kappa}$ and $\hbar\omega_\kappa$). In this case, the transition probability from the thermally populated manifold i to the manifold f is given by [22]

$$W^{(2)} = \frac{2\Delta_\lambda \Delta_\kappa}{\hbar^2} \sum_f \sum_i P_i \left| S_{fi}^{\vec{\kappa}\vec{\lambda}} \right|^2 D(\omega_{fi} - \omega_\lambda - \omega_\kappa) \quad (1)$$

where

$$S_{fi}^{\vec{\lambda}\vec{\kappa}} = \sum_m \left[\frac{(\vec{\kappa} \cdot \vec{\mu}_{fm})(\vec{\lambda} \cdot \vec{\mu}_{mi})}{\omega_{mi} - \omega_\kappa} + \frac{(\vec{\lambda} \cdot \vec{\mu}_{fm})(\vec{\kappa} \cdot \vec{\mu}_{mi})}{\omega_{mi} - \omega_\lambda} \right] \quad (2)$$

Table 2. Calculated components of transition dipole moments (atomic units) between various electronic states of allene.[a]

States	*x*	*y*	*z*	States	*x*	*y*	*z*
1^1A_2–1^1A_1	−0.0145	0	0	4^1A_1–2^1E	0	0.1668	0
2^1A_1–1^1A_2	0.0191	0	0	1^1A_2–2^1E	0	0	0
2^1B_1–1^1A_2	−1.1383	0	0	1^1B_2–2^1E	0	0	−0.0373
3^1A_1–1^1A_2	−0.2776	0	0	2^1A_2–2^1E	0	0	−0.6563
3^1B_1–1^1A_2	−2.2298	0	0	2^1B_2–2^1E	0	0	2.7655
4^1A_1–1^1A_2	0.0025	0	0	3^1A_2–2^1E	0	0	−2.9203
1^1B_2–1^1A_1	−0.9172	0	0	3^1E–2^1E	6.0860	0	0
1^1B_1–1^1B_2	0	0	0	4^1E–2^1E	0.3726	0	0
2^1A_1–1^1B_2	0.1471	0	0	5^1E–2^1E	−0.7667	0	0
2^1B_1–1^1B_2	−0.0514	0	0	3^1E–1^1A_1	0	0.3584	0
3^1A_1–1^1B_2	−3.9511	0	0	1^1B_1–3^1E	0	0	0
3^1B_1–1^1B_2	0.4427	0	0	2^1A_1–3^1E	0	0.1177	0
4^1A_1–1^1B_2	0.1988	0	0	2^1B_1–3^1E	0	−0.4893	0
2^1A_2–1^1A_1	−0.0123	0	0	3^1A_1–3^1E	0	0.2084	0
1^1B_1–2^1A_2	0	0	0	3^1B_1–3^1E	0	−0.1052	0
2^1A_1–2^1A_2	−0.0190	0	0	4^1A_1–3^1E	0	−0.4858	0
2^1B_1–2^1A_2	1.8349	0	0	1^1A_2–3^1E	0	0	0
3^1A_1–2^1A_2	0.2200	0	0	1^1B_2–3^1E	0	0	−0.2325
3^1B_1–2^1A_2	2.4422	0	0	2^1A_2–3^1E	0	0	0.4424
4^1A_1–2^1A_2	0.0007	0	0	2^1B_2–3^1E	0	0	−0.2200
2^1B_2–1^1A_1	−0.3880	0	0	3^1A_2–3^1E	0	0	0.1634
1^1B_1–2^1B_2	0	0	0	1^1E–3^1E	0.0872	0	0
2^1A_1–2^1B_2	−4.1819	0	0	2^1E–3^1E	6.0860	0	0
2^1B_1–2^1B_2	0.0367	0	0	4^1E–3^1E	−6.8568	0	0
3^1A_1–2^1B_2	0.4158	0	0	5^1E–3^1E	−0.3356	0	0
3^1B_1–2^1B_2	−0.1564	0	0	4^1E–1^1A_1	0	−0.1463	0
4^1A_1–2^1B_2	−0.1801	0	0	1^1B_1–4^1E	0	0	0
3^1A_2–1^1A_1	0.0242	0	0	2^1A_1–4^1E	0	0.2004	0
1^1B_1–3^1A_2	−3.2046	0	0	2^1B_1–4^1E	0	0.0332	0
2^1A_1–3^1A_2	0.2237	0	0	3^1A_1–4^1E	0	−0.2136	0
2^1B_1–3^1A_2	1.5203	0	0	3^1B_1–4^1E	0	0.2941	0
3^1A_1–3^1A_2	−0.2579	0	0	4^1A_1–4^1E	0	−0.0471	0
3^1B_1–3^1A_2	−2.0343	0	0	1^1A_2–4^1E	0	0	0
4^1A_1–3^1A_2	0.0117	0	0	1^1B_2–4^1E	0	0	−0.1403
1^1E–1^1A_1	0	−0.6663	0	2^1A_2–4^1E	0	0	0.0164
1^1B_1–1^1E	0	0	0	2^1B_2–4^1E	0	0	0.2739
2^1A_1–1^1E	0	−2.9630	0	3^1A_2–4^1E	0	0	−0.2862
2^1B_1–1^1E	0	2.0239	0	1^1E–4^1E	0.0872	0	0
3^1A_1–1^1E	0	−0.4686	0	2^1E–4^1E	0.3726	0	0
3^1B_1–1^1E	0	−0.6234	0	3^1E–4^1E	−6.8568	0	0
4^1A_1–1^1E	0	0.5973	0	5^1E–4^1E	9.7142	0	0
1^1A_2–1^1E	0	0	0	5^1E–1^1A_1	0	−0.1426	0
1^1B_2–1^1E	0	0	3.0541	1^1B_1–5^1E	0	0	0
2^1A_2–1^1E	0	0	−2.6395	2^1A_1–5^1E	0	−0.8974	0
2^1B_2–1^1E	0	0	−0.1169	2^1B_1–5^1E	0	0.8394	0
3^1A_2–1^1E	0	0	0.51984	3^1B_1–5^1E	0	−0.2665	0
2^1E–1^1E	−3.9633	0	0	4^1A_1–5^1E	0	0.5065	0
3^1E–1^1E	0.0872	0	0	1^1A_2–5^1E	0	0	0.2667
4^1E–1^1E	0.1018	0	0	1^1B_2–5^1E	0	0	0.9364
5^1E–1^1E	−0.0480	0	0	2^1A_2–5^1E	0	0	−0.9802
2^1E–1^1A_1	0	−0.2908	0	2^1B_2–5^1E	0	0	−0.0491
1^1B_1–2^1E	0	0	0	3^1A_2–5^1E	0	0	0.1921
2^1A_1–2^1E	0	0.5644	0	1^1E–5^1E	−0.0480	0	0
2^1B_1–2^1E	0	1.0900	0	2^1E–5^1E	−0.7667	0	0

(*continued*)

Table 2. Continued.

States	x	y	z	States	x	y	z
3^1A_1–2^1E	0	−2.5236	0	3^1E–5^1E	−0.3356	0	0
3^1B_1–2^1E	0	2.9563	0	4^1E–5^1E	9.7142	0	0
				3^1A_1–5^1E	0	−0.1307	0

[a]The transition dipole moments are calculated with the state-average CASSCF (4,11)/6-311(2+)G** method with equal weights for 22 electronic states, and the molecule is represented within D_{2d} symmetry.

Table 3. Optimized geometries of various electronic states of allene.

State[a]					
D_{2d}	D_2	R(CC)	R(CH)	CCH	HCCH
1^1A_1	1^1A	1.300	1.083	121.4	90.0
2^1A_1	3^1A	1.323	1.076	119.5	46.9
1^1B_2	2^1B_1	1.335	1.077	120.2	52.6
2^1E	2^1B_3	1.335	1.079	120.5	77.4
	2^1B_2	1.324	1.079	120.6	52.6
1^1A_2	3^1B_1	1.324	1.079	120.2	51.6
2^1B_1	4^1A	1.325	1.078	120.3	54.0
3^1A_1	5^1A	1.342	1.078	120.2	79.3
$C_3H_4^+$	$^2B_2$	1.314	1.093	121.0	49.3

[a]The character for each electronic state can be found in the third column of table 1.

Table 4. Calculated vibrational frequencies (cm^{-1}) of allene and allene cation.

Mode	Sym.	Allene[a]	Cation	Assignment
ν_1	a_1	3005 (3014)	2961	CH sym stretch
ν_2	a_1	1425 (1443)	1343	CH_2 sym sciss.
ν_3	a_1	1068 (1072)	1027	CC sym stretch
ν_4	b_1	852 (865)	774 (756)[b]	CH_2 twisting
ν_5	b_2	3001 (3007)	2945	CH stretch
ν_6	b_2	1976 (1959)	1576 (1802)[b]	CC asym stretch
ν_7	b_2	1370 (1395)	1298	CH_2 asym sciss.
ν_{8-9}	e	3073 (3086)	3037	CH asym stretch
			3037	
ν_{10-11}	e	980 (999)	960	CH_2 in-plane wagging
			898	
ν_{12-13}	e	834 (841)	876	CH_2 out-of-plane wagging
			785	
ν_{14-15}	e	359 (352)	329	CCH bend
			311	

[a]In parentheses: experimental frequencies from [13].
[b]In parentheses: experimental frequencies from [42].

and

$$\Delta_\lambda = \frac{2\pi n_\lambda \omega_\lambda}{L^3}, \tag{3}$$

in which m denotes intermediate states, P_i is the Boltzmann distribution function, $\vec{\mu}_{fm} = \langle f | \vec{\mu} | m \rangle$ is the transition dipole moment for the transition of $m \to f$, n_λ represents photon number, $\hbar\omega_\lambda$ is the photon energy in the mode λ, L is the length of a cubic box for radiation fields, and $D(\omega_{fi} - \omega_\lambda - \omega_\kappa)$ denotes the line shape function. Details of the further derivation are attached in the Appendix to this paper. The data needed for calculations include excited state energies (table 1) and transition dipole moments for various one-photon transitions (table 2). The computed numerical results of two-photon transition probabilities are listed in table 1.

4. Results and discussion

4.1. *REMPI spectroscopy*

A typical TOF mass spectrum of allene via $2+1$ REMPI is shown in figure 1(a), where the 3^1A_1 (5^1A) [under the symmetry group of D_{2d} (D_2)] origin band is the intermediate state two-photon excited by a focused laser at 294.87 nm. The most abundant fragmentary ions are C^+, C_2^+ and $C_3H_3^+$. The $C_3H_4^+$ signal is very weak indicating that most of parent ions dissociate into daughter fragments either directly or by absorbing extra photons. When the two-photon energy of the laser is above the *IE* of allene, the $C_3H_4^+$ signal is enhanced as shown in figure 1(b). Figure 2 shows a $2+1$ REMPI composite spectrum of allene at 7.4–10.5 eV. The signal intensity in the composite spectrum of figure 2 was not corrected for changes in the laser energy, but was normalized to the same value in the common wavelength regions of dyes.

Evidence given below shows that the observed spectra result from a $2+1$ REMPI process. First, no excited singlet state of allene has been reported to lie between 3.7 and 5.3 eV [44] (in agreement with our calculation that the first excited singlet state is >5.84 eV, table 1). This rules out the possibility of $1+2$ REMPI. Second, a power-dependence measurement in our experiment for allene, similar to the previous study of the propyne

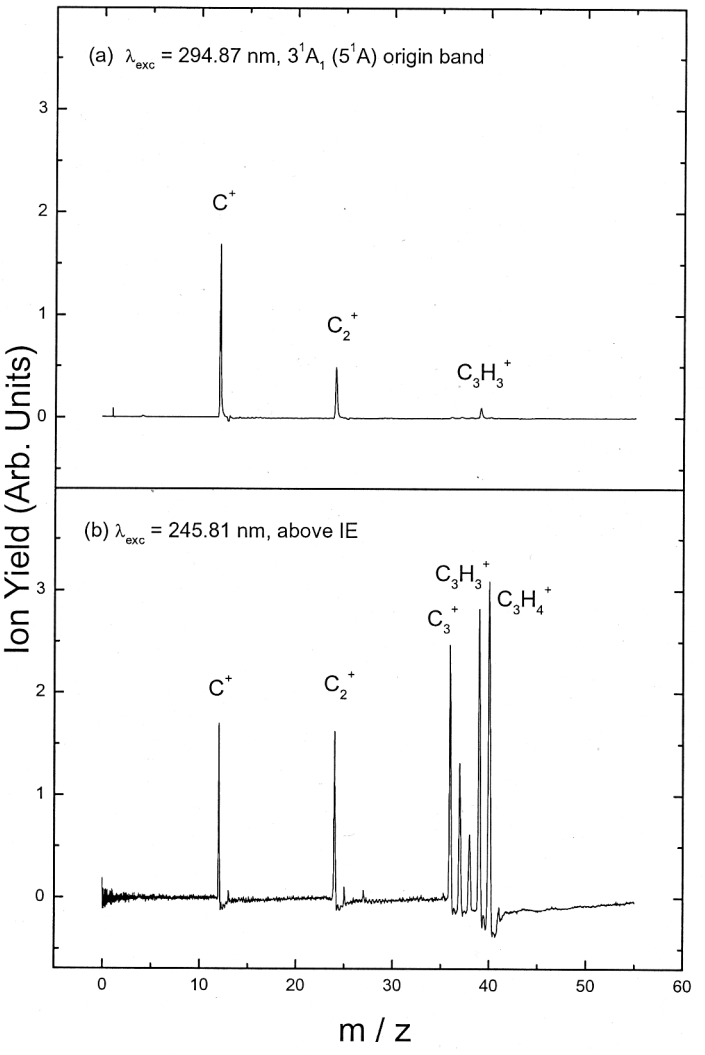

Figure 1. Typical TOF mass spectra of allene excited at (a) 294.87 nm of the 5^1A origin band, and (b) 245.81 nm where two-photon energy is above the ionization energy of allene.

molecule [21], confirms the two-photon resonance process.

We have determined the symmetry of the excited vibronic states of allene with polarization-ratio measurements using linearly and circularly polarized lasers. The observed $2+1$ REMPI spectra of allene with different laser polarizations are shown in figure 3. To obtain better precision, the polarization-ratio measurement for a particular transition was carried out with the laser wavelength fixed on the top of the transition, as mentioned in the experimental section. In a supersonic-jet expansion, most of the allene molecules are initially in the vibrational ground state prior to laser excitation. According to the two-photon theory for a molecule with D_{2d} symmetry, $\Omega < 3/2$ for the transition from the A_1 ground state to the A_1 excited state, and $\Omega = 3/2$ for transitions to the B_1, B_2 and E states.

Owing to spectral congestion and the small signal-to-noise ratios in the present experiment, the polarization-ratio measurement for allene was more difficult than in the previous study of propyne [21]. The polarization-ratio measurements for the peaks above 74 500 cm^{-1} (figure 3(b)) were too weak to be accurately determined. For the peaks below 74 500 cm^{-1}, we take $\Omega = 0.8$ as a threshold. Peaks with $\Omega < 0.8$ are regarded as of A_1 symmetry, and those with $\Omega > 0.8$ are of other symmetries. The observed vibronic transitions and their corresponding polarization ratios (Ω) of allene are listed in table 5.

4.2. *Calculations*

According to table 3, the most significant change in the geometry of excited electronic states (>7 eV) of allene

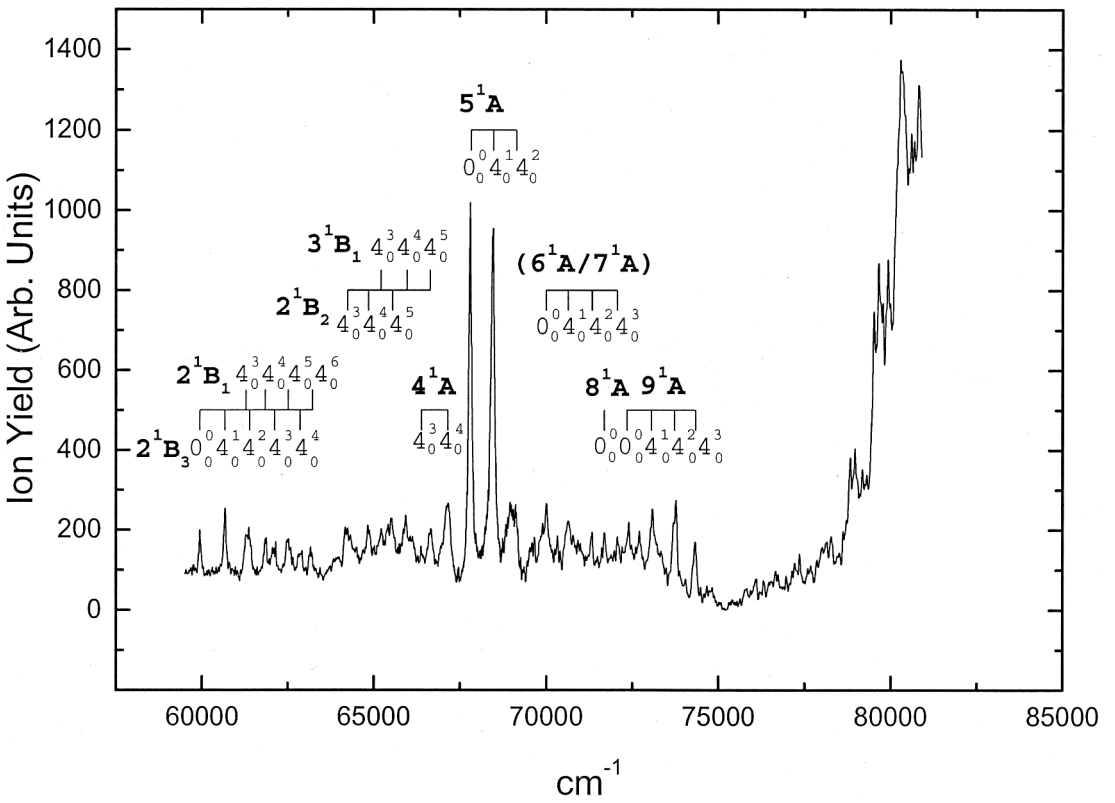

Figure 2. Composite 2+1 REMPI spectrum of allene at 7.4–10.5 eV. Linearly polarized laser light was employed for the observation. The symmetry representations are within a D_2 group.

compared to the ground state 1^1A_1 (1^1A) [under the symmetry group D_{2d} (D_2)] concerns the dihedral HCCH angle. In the ground state, this angle is 90° (D_{2d} symmetry). As discussed in the previous study [4], the molecule is planar for the first excited (π, π^*) state (not shown in table 2), so the angle changes to 0° (D_{2h} symmetry). In the cation and the Rydberg states of allene, the CH_2 twisting is smaller. The dihedral angle is in the range of 50°–80°, and the molecule possesses only D_2 symmetry. Since both a_1 and b_1 irreducible representations of a D_{2d} point group correspond to the fully symmetric irreducible representation a in D_2, the active vibrational modes to appear in the vibronic spectrum of allene in the present supersonic-jet experiment are of a_1 and b_1 symmetries under a D_{2d} group. As a theoretical result, the normal mode corresponding to the CH_2 twisting, ν_4 (b_1, 852 cm^{-1} in allene and 774 cm^{-1} in cation), exhibits the largest displacement (ΔQ_4) and should be the most active vibrational mode in the vibronic spectra. The other active modes with a_1 symmetry include the CH symmetric stretching (ν_1), CH_2 symmetric scissoring (ν_2), and CC symmetric stretching (ν_3) [45]. Since the changes in the CC and CH bond lengths and the HCH angles are relatively small upon electronic excitation, the $\Delta Q_1 - \Delta Q_3$ displacements are much smaller than ΔQ_4. Therefore, the ν_4 mode dominates the vibrational progressions in the vibronic spectrum of allene.

Judging from the calculated vibrational frequencies for the allene cation (table 4), which were taken as approximate frequencies for Rydberg states, the normal mode distortion (change of vibrational frequencies from the ground to Rydberg states) is not very strong. The largest distortion, from 1976 to 1576 cm^{-1}, is found for ν_6 (b_2, CC asymmetric stretch). This mode is not fully symmetric in D_2 and cannot appear in the REMPI spectrum of the present experiment. The distortion can result in non-zero Franck–Condon factors for 6_0^n vibronic transitions with even values of n. However, the calculated Franck–Condon factor for the 6_0^2 transition, 6.3×10^{-3}, is 157.7 times smaller than that for 6_0^0, indicating very low activity of ν_6 in the spectrum. Hence, the distorted, but not displaced, normal modes were excluded from our calculation. On the other hand, the displaced ν_1–ν_4 modes also exhibit some distortion, and the calculations of Franck–Condon factors for these four normal modes were carried out for both displaced and distorted harmonic oscillators. We used

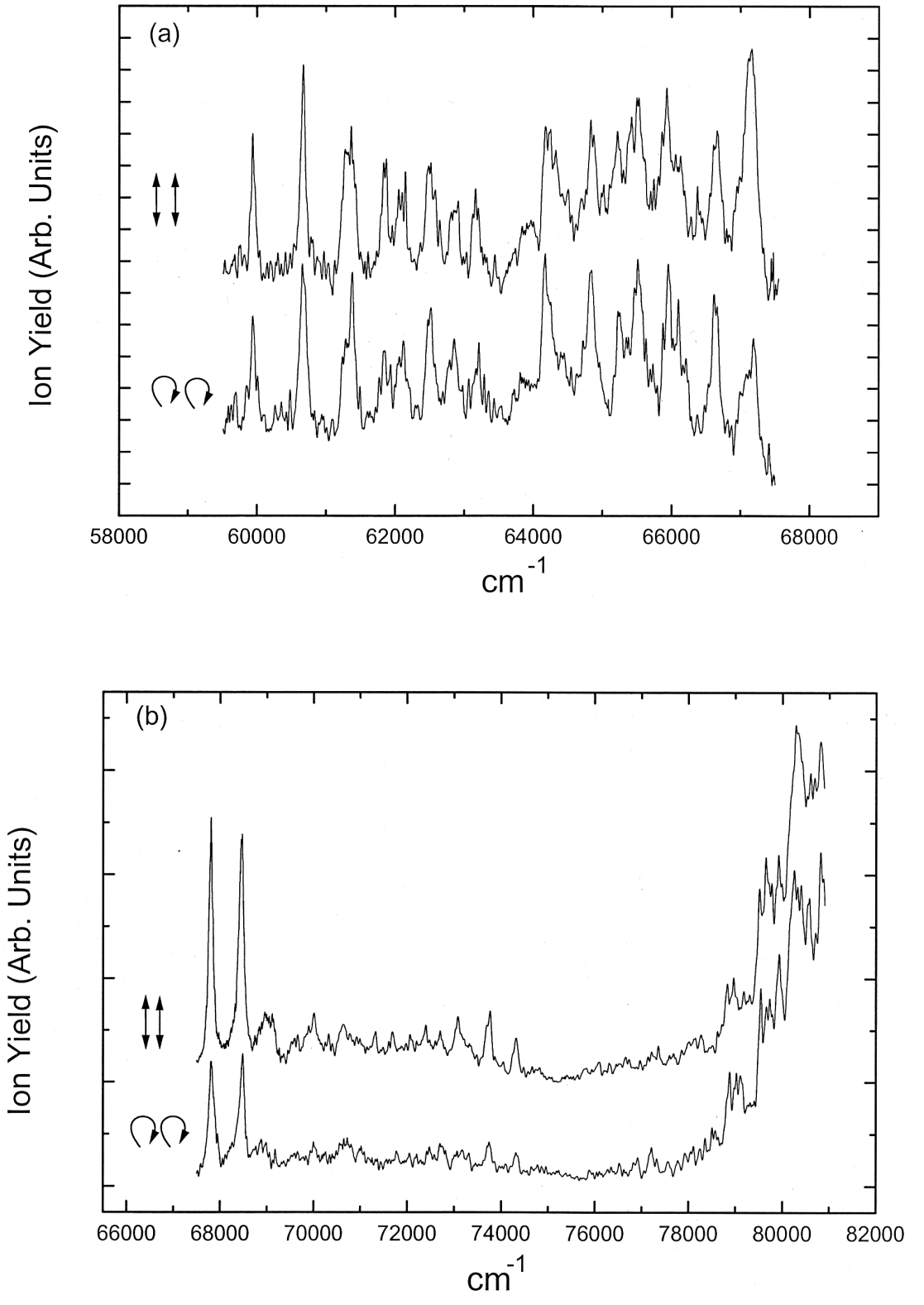

Figure 3. (a–b) Polarization dependence for the 2 + 1 REMPI signals of allene at 7.4–10.5 eV. Spectra with linearly (upper trace) and circularly (lower trace) polarized excitations are laid out for comparison. The intensity scale in (a) is 5 times magnified with respect to that in (b) for clearer visualization of the spectral features.

Table 5. Observed frequencies, polarization-ratios, state assignments, and vibrational intervals of vibronically excited allene studied by 2 + 1 REMPI spectroscopy.

Observed frequency[a]	Ω	Assignment (in D_2)[b]	Calc. energy[c]	Vibrational interval[d]				
59937 (7.43)	0.87	$2^1B_3\ 0_0^0$	7.30	*				
60667 (7.52)	0.87	$2^1B_3\ 4_0^1$	7.40	730				
61281 (7.60)	0.98	$2^1B_1\ 4_0^3/3^1A\ 4_0^4$	7.47/7.55					
61379 (7.61)	0.95	$2^1B_3\ 4_0^2$	7.50	712				
61838 (7.67)	0.97	$2^1B_1\ 4_0^4/3^1A\ 4_0^5$	7.56/7.65		557			
62109 (7.70)	1.1	$2^1B_3\ 4_0^3$	7.59	730				
62507 (7.75)	1.1	$2^1B_1\ 4_0^5/3^1A\ 4_0^6$	7.66/7.74		669			
62858 (7.79)	1.25	$2^1B_3\ 4_0^4$	7.69	749				
63219 (7.84)	1.24	$2^1B_1\ 4_0^6/3^1A\ 4_0^7$	7.75/7.84		712			
64245 (7.97)	1.3	$2^1B_2\ 4_0^3$	7.95					
64849 (8.04)	1.18	$2^1B_2\ 4_0^4$	8.05			604		
65215 (8.08)	0.92	$3^1B_1\ 4_0^3$	8.12					
65549 (8.13)	1.05	$2^1B_2\ 4_0^5$	8.14			700		
65972 (8.18)	1.06	$3^1B_1\ 4_0^4$	8.21				757	
66385 (8.23)	0.57[e]	$4^1A\ 4_0^3$	8.29					
66634 (8.26)	0.93	$3^1B_1\ 4_0^5$	8.31				662	
67152 (8.33)	0.50[e]	$4^1A\ 4_0^4$	8.39					767
67827 (8.41)	0.38[e]	$5^1A\ 0_0^0$	8.34	*				
68470 (8.49)	0.25[e]	$5^1A\ 4_0^1$	8.43	643				
69139 (8.57)	0.53[e]	$5^1A\ 4_0^2$	8.52	669				
70010 (8.68)	0.58[e]	$3d(6^1A/7^1A)\ 0_0^0$	(8.53/8.56)[f]		*			
70637 (8.76)	0.71[e]	$3d(6^1A/7^1A)\ 4_0^1$			627			
71329 (8.84)	0.44[e]	$3d(6^1A/7^1A)\ 4_0^2$			692			
71686 (8.89)	0.54[e]	$4p(8^1A)\ 0_0^0$	(8.97)[f]			*		
72061 (8.93)	0.50[e]	$3d(6^1A/7^1A)\ 4_0^3$			732			
72345 (8.97)	0.42[e]	$4p(9^1A)\ 0_0^0$	(8.98)[f]				*	
73053 (9.06)	0.38[e]	$4p(9^1A)\ 4_0^1$					708	
73723 (9.14)	0.39[e]	$4p(9^1A)\ 4_0^2$					670	
74332 (9.22)	0.39[e]	$4p(9^1A)\ 4_0^3$					609	
74715 (9.26)		4p/4d	(9.05–9.20)[f]					
75401 (9.35)		4p/4d						
75872 (9.41)		4p/4d						
76066 (9.43)		4p/4d						
76499 (9.48)		4p/4d						
76679 (9.51)		4p/4d						
77185 (9.57)		4p/4d						
77364 (9.59)		4p/4d						
77855 (9.65)		4p/4d						

[a]Observed frequencies are given in cm^{-1} and in eV (in parentheses).
[b]All excitations are from the ground 1^1A_1 (1^1A) (π) state. The character for each electronic state can be found in the third column of table 1.
[c]Excitation energies in eV calculated at the MRCI level, unless mentioned otherwise.
[d]In cm^{-1}. * represents origin band.
[e]Fully symmetric transition according to the polarization ratio.
[f]Vertical excitation energies in eV calculated at the TDDFT level.

the vibrational frequencies of allene cation to evaluate the vibrational spacings in the calculated vibronic spectra. Among those, the most important is the CH_2 twisting ($\nu_4 = 774\,cm^{-1}$) as mentioned above. As will be seen in the following section, experimental vibrational spacings somewhat differ from the cation frequency and between different Rydberg states. Nevertheless, the cation values provide a fair estimation.

Comparison of the excitation energies computed by different theoretical methods shows a satisfactory agreement between the results of *ab initio* MO and TDDFT (table 1), especially, for the Rydberg states. For instance, for the 1^1B_2 (2^1B_1) state the TDDFT vertical excitation energy, 7.47 eV, is 0.15 eV lower than that obtained earlier at EOM-CCSD [4]. At the MRCI level, the energy of the most intense peak 4_0^4 is 7.56 eV, also close to the vertical energies calculated by the EOM-CCSD and TDDFT methods. In general, TDDFT predicts lower transition energies: 7.86 eV for 2^1A_2 (3^1B_1) versus 8.05 eV at EOM-CCSD and 8.21 eV for the 4_0^4 peak at MRCI, 7.87 eV for 2^1B_1 (4^1A) versus 8.06 eV (EOM-CCSD) and 8.29 eV (4_0^3, MRCI), 7.94 eV for 3^1A_1 (5^1A) versus 8.27 eV (EOM-CCSD) and 8.34 (0_0^0 origin band, MRCI), 8.33 and 8.40 eV for 3^1E and 2^1B_2 versus 8.46 and 8.61 eV, respectively, at EOM-CCSD. For the 2^1E state, the TDDFT and EOM-CCSD vertical energies also agree to each other within 0.2 eV, but a comparison with the MRCI results is complicated, since the E state splits into two components, B_2 and B_3, which exhibit the most intense transitions at 8.05 eV (2^1B_2 4_0^4) and 7.30 eV (2^1B_3 0_0^0), respectively. Larger discrepancies are found for the valence π–π^* transitions, where the TDDFT values differ from the *ab initio* MO by up to 0.6 eV. A similar trend was reported by us earlier for propyne [21], and we concluded that the MRCI method appears to give more accurate energies for the valence excited states than TDDFT.

According to the calculated two-photon intensities (table 1), the strongest band in the spectra should correspond to the $3^1A_1(5^1A)(3p_{x,y}) \leftarrow 1^1A_1(1^1A)(\pi)$ (i.e. $3p_{x,y} \leftarrow \pi$) transition. The intensities for the $2^1E(2^1B_3 + 2^1B_2)(3p_z) \leftarrow 1^1A_1(1^1A)(\pi)$ (i.e. $3p_z \leftarrow \pi$) transitions are about two times weaker in the circularly polarized laser measurement, and five times weaker for linearly polarized light. The $2^1A_1(3^1A)(\pi^*) \leftarrow 1^1A_1(1^1A)(\pi)$ (i.e. $\pi^* \leftarrow \pi$) band has comparable intensities with those for $2^1E(2^1B_3 + 2^1B_2) \leftarrow 1^1A_1(1^1A)$, while those for the transitions from $1^1A_1(1^1A)(\pi)$ to $1^1B_2(2^1B_1)(\pi^*/3p_{x,y})$, $2^1A_2(3^1B_1)(3p_{x,y})$, and $2^1B_1(4^1A)$ $(3p_{x,y})$ are expected to be weaker. Within the same electronic transition, the vibrational intensity distribution depends on Franck–Condon factors which, in turn, are mostly dominated by the CH_2 twisting mode, ν_4. When the dihedral angle in the excited state changes to $\sim 50^\circ$ [$3^1A(\pi^*)$, $2^1B_1(\pi^*/3p_{x,y})$, $2^1B_2(3p_z)$, $3^1B_1(3p_{x,y})$, and $4^1A(3p_{x,y})$ with the representations in D_2], the displacement of ΔQ_4 is large. Therefore, the vibronic spectrum should spread over a broad energy range, and the 4_0^3–4_0^5 transitions have the maximum intensities in the vibrational progression. On the other hand, in the $2^1B_3(3p_z)$ and $5^1A(3p_{x,y})$ states (in D_2) where the dihedral angle change is much smaller (to $\sim 80^\circ$), ΔQ_4 is minor, and the 0_0^0 origin-band transition dominates in the intensity distribution, with smaller contributions from 4_0^1, 4_0^2, etc. Figure 4 shows the calculated vibronic spectra for allene with different laser polarizations, (a) linearly and (b) circularly polarized laser light.

4.3. *Assignment of experimental spectra*

Based on the satisfactory agreement in the theoretical results between *ab initio* MO and TDDFT, the computed excitation energies and molecular geometries should be reliable. As demonstrated in previous studies of ethylene [18, 19], vinyl radical [46, 47], vinyl chloride [48, 49], acetone [50–52], allyl radical [26, 53], and 2-methylallyl radical [28], we have successfully applied the calculated Franck–Condon factors to assist spectroscopic assignment for experimental vibronic spectra. In this study, we have tentatively assigned most of the observed two-photon transitions of allene (table 5), although in the calculated spectrum we considered only a harmonic oscillator approximation without vibronic couplings. We regard our spectral treatment in the present work to the observed vibrationally resolved REMPI spectra of allene as a primary step. More terms in the interaction Hamiltonian can be further taken into account in future.

Also, in this assignment we assume that the calculated MRCI energies can deviate from actual values up to 0.15 eV. The computed intensity distribution is very sensitive to small changes of the HCCH dihedral angle, and therefore can also deviate from experiment. With the aid of calculations, peak positions can be located, and the calculated Franck–Condon factors have provided useful intensity information for the vibrational assignment. The measured polarization-ratios indicate the excited vibronic symmetry are helpful in the spectroscopic assignment. It is noted, however, that in case an excited state is strongly predissociative, the corresponding vibronic transition is absent in the observed REMPI spectrum. In the following analysis, the discrepancy in the calculated strong peaks, such as the $2^1A_1(3^1A)(\pi^*) \leftarrow 1^1A_1(1^1A)(\pi)$ transition, could be in part due to this reason.

The strongest peaks at 67 827 and 68 470 cm^{-1} are attributed to the 0_0^0 and 4_0^1 vibronic transitions to the

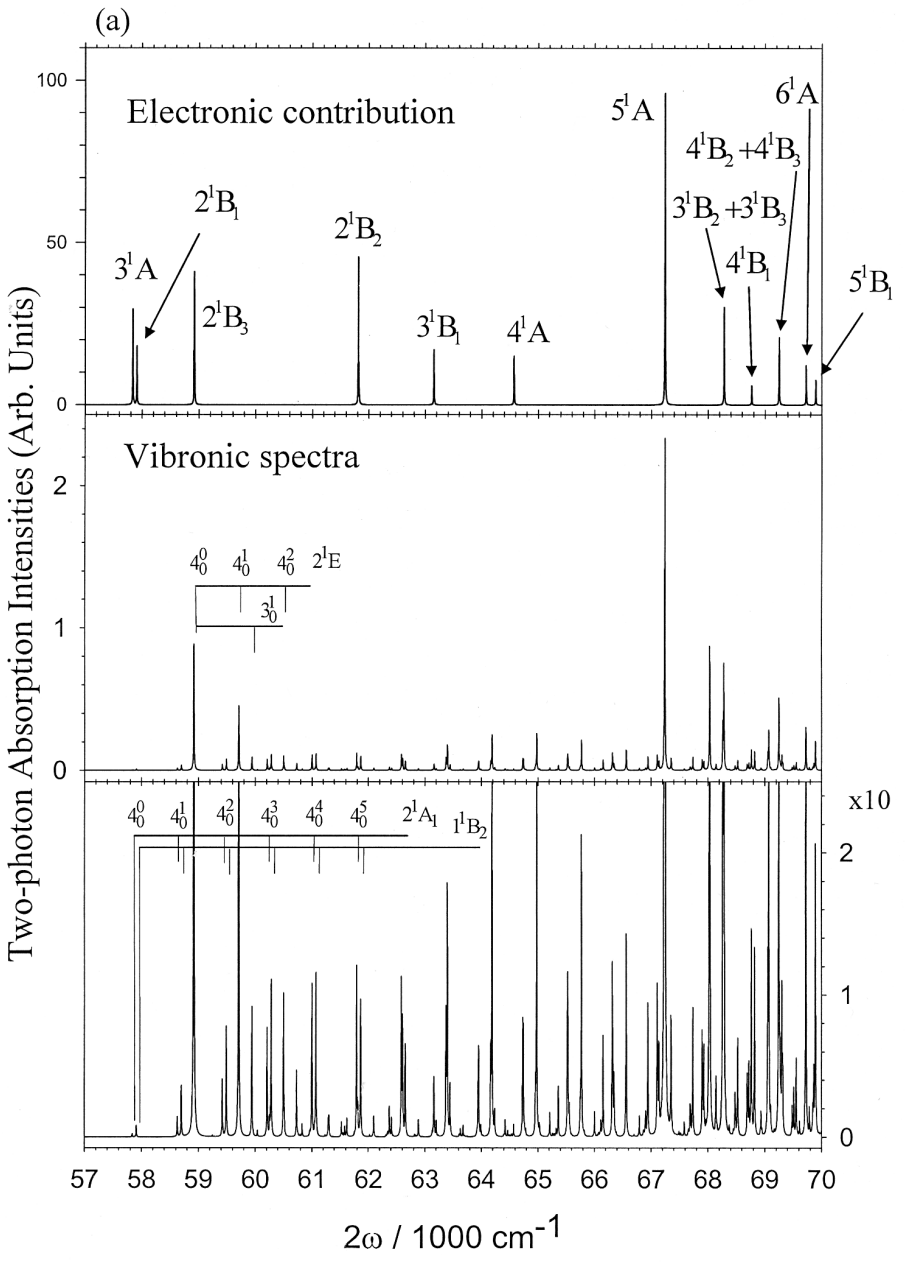

Figure 4. Calculated vibronic spectra of allene using (a) linearly and (b) circularly polarized laser light. The top panel represents the two-photon electronic transition probabilities to various excited electronic states. The symmetry representations are within a D_2 group. The vibronic spectra in the middle and bottom panels include the electronic contribution and calculated Franck–Condon factors with the scale of the bottom panel being 10 times expanded from that of the middle.

$3^1A_1(5^1A)(3p_{x,y}) \leftarrow 1^1A_1(1^1A)(\pi)$ electronic state. The calculated adiabatic excitation energy without zero point energy correction, 8.34 eV, closely matches the experimental value of 8.41 eV. The measured ν_4 vibrational frequency is 643–669 cm^{-1}, more than 100 cm^{-1} lower than the calculated value for allene cation. The second prominent spectral feature is a series of intense peaks starting from 59 937 cm^{-1} and spaced by 712–749 cm^{-1}. Based on their intensity, we are inclined to assign them to a vibrational progression in the $2^1E(2^1B_3)(3p_z) \leftarrow 1^1A_1(1^1A)(\pi)$ transition. Then, the calculated adiabatic excitation energy, 7.30 eV, underestimates the measured origin band by 0.13 eV, i.e. within the expected accuracy of our MRCI calculations. According to the theoretical results, the 0_0^0 and 4_0^1 vibronic peaks should exhibit the largest

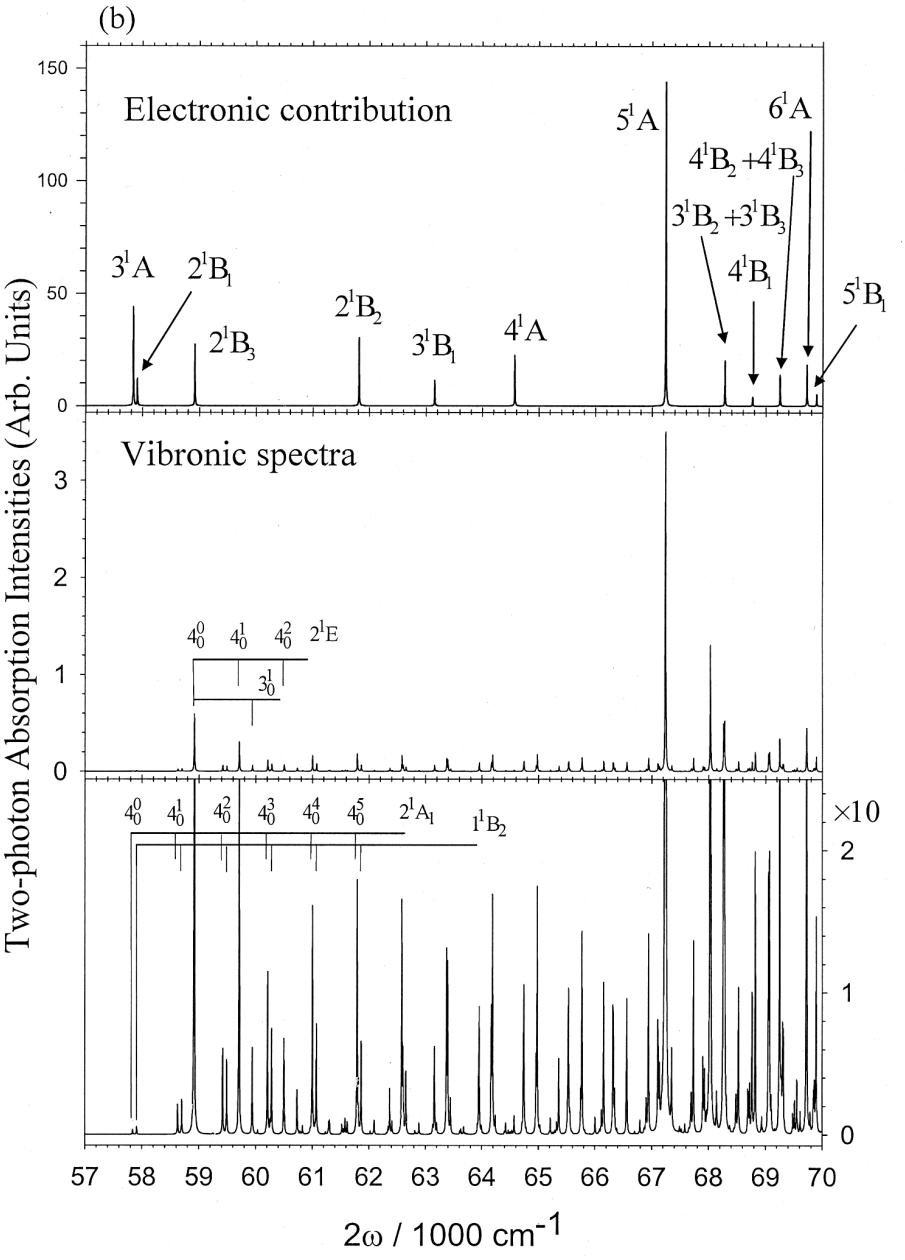

Figure 4. Continued.

intensities with a ratio 2.7:1. This is not the case in the observed spectra where the first three peaks in the progression show similar intensities and the 4_0^1 band is the strongest one. This discrepancy might be due to small underestimation of the CH_2 twisting in the $2^1E(2^1B_3)(3p_z) \leftarrow 1^1A_1(1^1A)(\pi)$ excitation as mentioned above. The discrepancy could also stem from the lower power at the edge of the laser dye used to excite the 0_0^0 band.

The series of peaks starting from 61 281 cm^{-1} with uneven vibrational spacing (557, 669, and 712 cm^{-1}) can be assigned to a mixture of two electronic transitions, to $1^1B_2(2^1B_1)(\pi^*/3p_{x,y}) \leftarrow 1^1A_1(1^1A)(\pi)$ and $2^1A_1(3^1A)(\pi^*) \leftarrow 1^1A_1(1^1A)(\pi)$. According to the calculations, both states should have intense vibronic peaks in the experimental energy range of 7.5–7.8 eV. The $2^1A_1(3^1A)(\pi^*) \leftarrow 1^1A_1(1^1A)(\pi)$ transition is calculated to have a larger two-photon intensity, but measured polarization ratio does not support the assignment to a fully symmetric transition. The presence of the $1^1B_2(2^1B_1)(\pi^*/3p_{x,y}) \leftarrow 1^1A_1(1^1A)(\pi)$ transition in this wavelength region could be responsible for the change

in polarization ratios as well as for the observed alteration in the vibrational spacing.

The vibrational progression at 64 245, 64 849, and 65 549 cm^{-1} is assigned to the $2^1E(2^1B_2)(3p_z) \leftarrow 1^1A_1(1^1A)(\pi)$ transition, while that at 65 215, 65 972, and 66 634 cm^{-1} to $2^1A_2(3^1B_1)(3p_{x,y}) \leftarrow 1^1A_1(1^1A)(\pi)$. According to the measured polarization ratios, the excited states of the bands at 66 385 and 67 152 cm^{-1} possess a full symmetry. Hence, we assign them to the $(\pi,3p_{x,y})$ (i.e. $2^1B_1(4^1A)$) electronic state. The vibrational quantum numbers for the vibronic transition shown in table 5 were chosen by using the ones with largest calculated Franck–Condon factors.

As mentioned before, the theoretical energies agree with the observed band positions within 0.1 eV. The peaks at 70 010, 70 637, 71 329, and 72 061 cm^{-1} are due to the $3^1B_1(6^1A)(3d_{xz,yz}) \leftarrow 1^1A_1(1^1A)(\pi)$ and $4^1A_1(7^1A)(3d_{xz,yz}) \leftarrow 1^1A_1(1^1A)(\pi)$ electronic transitions, which have very similar excitation energies at the TDDFT level. We have also assigned the bands at 71 686 and 72 345–74 332 cm^{-1} to the fully symmetric $(\pi, 4p_{x,y})$ states (i.e. $4^1B_1(8^1A)(4p_{x,y}) \leftarrow 1^1A_1(1^1A)(\pi)$ and $5^1A_1(9^1A)(4p_{x,y}) \leftarrow 1^1A_1(1^1A)(\pi)$ transitions. Finally, the peaks from 74 715 to 77 855 cm^{-1} can be tentatively attributed to various $4p \leftarrow \pi$ and/or $4d \leftarrow \pi$ transitions. Note that the calculated TDDFT energies underestimate the experimental values by 0.3–0.5 eV. More accurate MRCI calculations for such highly excited states are not feasible.

It is worth mentioning that the observed spectra (figures 2 and 3) for Rydberg excited states are complicated by the presence of underlying continuum – a broad and feature-less spectrum due to the lowest excited (π, π^*) state. This state (^1A_g in D_{2h} symmetry) has a planar optimized geometry, so the CH_2 groups are twisted by 90° compared to the ground state structure. Our earlier calculations of Franck–Condon factors for vibronic transitions to this state showed that the underlying continuum should be spread over the very broad energy range of 6.0–13.5 eV [45].

5. Conclusions

We have observed 2 + 1 REMPI spectra of allene at 7.0−10.5 eV. The excited vibronic symmetry has been determined from polarization-ratio measurements. The REMPI spectra have been assigned as due to $\pi^* \leftarrow \pi$ and the $3p \leftarrow \pi$, $4s \leftarrow \pi$, $4p \leftarrow \pi$, and $4d \leftarrow \pi$ transitions to Rydberg electronic states based on the calculated vibronic energies and peak intensities using *ab initio* MO and time-dependent density functional theory. The strongest peaks in the spectra are observed at 67 827 and 68 470 cm^{-1} and correspond to the origin band and the 4_0^1 vibronic peak of the $3^1A_1(5^1A)(3p_{x,y}) \leftarrow 1^1A_1(1^1A)(\pi)$ band, respectively. These peaks can be suggested for monitoring the allene concentration by means of the REMPI spectroscopy in future kinetic measurements of chemical reactions of allene. Another important feature of the observed spectra includes three intense peaks at 59 937, 60 667, and 61 379 cm^{-1} assigned to vibronic excitations to the $(\pi, 3p_z)$ state (i.e. $2^1E(2^1B_3)(3p_z) \leftarrow 1^1A_1(1^1A)(\pi)$). Vibrational progressions related to the CH_2 twisting (ν_4 mode) have been observed for several excited states, such as 2^1B_3 $(\pi, 3p_z)$, 2^1B_1 $[(\pi, \pi^*)/(\pi, 3p_{x,y})]$, 3^1A (π, π^*), 2^1B_2 $(\pi, 3p_z)$, 3^1B_1, 4^1A and 5^1A $(\pi, 3p_{x,y})$, 6^1A and 7^1A $(\pi, 3d)$, and 9^1A $(\pi, 4p)$. Most regular vibrational spacing is found for 2^1B_3 and 5^1A, where the CH_2 twisting frequency is measured as 712–749 and 643–669 cm^{-1}, respectively.

The excitation energies calculated at the MRCI level agree with experimentally observed peak positions with the accuracy of 0.15 eV or better. The TDDFT energies are lower than the *ab initio* MO results by ~0.2 eV and the experimental values by 0.3–0.5 eV. In any case, the TDDFT method is the better choice for semi-quantitative theoretical studies of Rydberg excited states, especially, for the high-lying states and for large molecular systems. In MRCI or CASPT2 methods more and more vacant orbitals have to be included into the active space for the calculations of higher Rydberg states. On the contrary, TDDFT does not depend on the active space choice. Meanwhile, a proper basis set has to be used which includes diffuse functions describing the Rydberg orbitals with quantum numbers $n = 3, 4$.

We have also suggested a theoretical approach for the calculations of two-photon intensities and polarization ratios based on *ab initio* computed one-photon transition dipole moments to various electronic states as intermediates. The approach has been applied to predict the peak intensities and polarization ratios for Rydberg states of allene, and the results showed good agreement between theory and experiment.

Acknowledgments

This work is supported by National Science Council of ROC (Grants No. 92-2113-M-001-037 and No. 92-2113-M-002-039) and China Petroleum Corporation. JLC is grateful to Academia Sinica fellowship during his postdoctoral career at IAMS. We would like to thank Professor M. N. R. Ashfold for showing us the REMPI spectra of allene from the thesis of his student, Mr Ross Morgan.

Appendix

Nuclear correlation function

In the adiabatic approximation, i.e., $|i\rangle = |g\rangle|gu\rangle$, $|e\rangle = |e\rangle|ev\rangle$ and $|m\rangle = |e'\rangle|e'w\rangle$, equation (1) becomes

$$W_g^{(2)} = \sum_e W_{e\leftarrow g}^{(2)} \tag{A1}$$

where

$$W_{e\leftarrow g}^{(2)} = \frac{2\Delta_\lambda \Delta_\kappa}{\hbar^2} \sum_e \sum_{ev} \sum_{gu} P_{gu} |S_{ev,gu}^{\vec{\kappa}\vec{\lambda}}|^2 D(\omega_{ev,gu} - \omega_\lambda - \omega_\kappa) \tag{A2}$$

and

$$S_{ev,gu}^{\vec{\lambda}\vec{\kappa}} = \sum_{e'} \sum_{e'w} \left[\frac{(\vec{\kappa}\cdot\vec{\mu}_{ev,e'w})(\vec{\lambda}\cdot\vec{\mu}_{e'w,gu})}{\omega_{e'w,gu} - \omega_\kappa} + \frac{(\vec{\lambda}\cdot\vec{\mu}_{ev,e'w})(\vec{\kappa}\cdot\vec{\mu}_{e'w,gu})}{\omega_{e'w,gu} - \omega_\lambda} \right]. \tag{A3}$$

Here, we are interested in the case where the transition to the intermediate state $|e'w\rangle$ is always non-resonant. Then, one can apply the Placzek approximation to equation (A3) and it reduces to

$$S_{ev,gu}^{\vec{\lambda}\vec{\kappa}} = \sum_{e'} \sum_{e'w} \left[\frac{(\vec{\kappa}\cdot\vec{\mu}_{ev,e'w})(\vec{\lambda}\cdot\vec{\mu}_{e'w,gu})}{\omega_{e'g} - \omega_\kappa} + \frac{(\vec{\lambda}\cdot\vec{\mu}_{ev,e'w})(\vec{\kappa}\cdot\vec{\mu}_{e'w,gu})}{\omega_{e'g} - \omega_\lambda} \right]. \tag{A4}$$

Applying the Condon approximation to equation (A4) and using the closure relation $\sum_{e'w} |e'w\rangle\langle e'w| = 1$ lead to

$$S_{ev,gu}^{\vec{\lambda}\vec{\kappa}} = \sum_{e'} \left[\frac{(\vec{\kappa}\cdot\vec{\mu}_{ee'})(\vec{\lambda}\cdot\vec{\mu}_{e'g})}{\omega_{e'g} - \omega_\kappa} + \frac{(\vec{\lambda}\cdot\vec{\mu}_{ee'})(\vec{\kappa}\cdot\vec{\mu}_{e'g})}{\omega_{e'g} - \omega_\lambda} \right] \langle ev|gu\rangle = \langle ev|gu\rangle S_{eg}^{\vec{\lambda}\vec{\kappa}}, \tag{A5}$$

where

$$S_{eg}^{\vec{\lambda}\vec{\kappa}} = \sum_{e'} \left[\frac{(\vec{\kappa}\cdot\vec{\mu}_{ee'})(\vec{\lambda}\cdot\vec{\mu}_{e'g})}{\omega_{e'g} - \omega_\kappa} + \frac{(\vec{\lambda}\cdot\vec{\mu}_{ee'})(\vec{\kappa}\cdot\vec{\mu}_{e'g})}{\omega_{e'g} - \omega_\lambda} \right]. \tag{A6}$$

Here, for example, $\vec{\mu}_{ee'}$ denotes the electronic transition dipole moment and $\langle ev|gu\rangle$ represents the Franck–Condon overlap integral. Substituting equations (A5) into (A6) yields

$$W_{e\leftarrow g}^{(2)} = \frac{2}{\hbar^2} \Delta_\lambda \Delta_\kappa |S_{eg}^{\vec{\lambda}\vec{\kappa}}|^2 \sum_{ev} \sum_{gu} P_{gu} |\langle ev|gu\rangle|^2 \times D(\omega_{ev,gu} - \omega_\lambda - \omega_\kappa). \tag{A7}$$

We now assume that the line shape function can be given by Lorentzian function

$$D(\omega_{ev,gu} - \omega_\lambda - \omega_\kappa) = \frac{\gamma_{eg}/\pi}{(\omega_{ev,gu} - \omega_\lambda - \omega_\kappa)^2 + \gamma_{eg}^2} = \frac{1}{2\pi} \int_{-\infty}^{\infty} dt\, e^{it(\omega_{ev,gu} - \omega_\lambda - \omega_\kappa) - |t|\gamma_{eg}}, \tag{A8}$$

where γ_{ba} denotes the electronic dephasing rate constant and we have neglected the vibrational contribution to γ_{eg} for simplicity. Substituting equations (A8) into (A7) leads to

$$W_{e\leftarrow g}^{(2)} = \frac{\Delta_\lambda \Delta_\kappa}{\pi\hbar^2} |S_{eg}^{\vec{\lambda}\vec{\kappa}}|^2 \sum_{ev} \sum_{gu} \int_{-\infty}^{\infty} dt\, P_{gu} |\langle ev|gu\rangle|^2 \times e^{it(\omega_{ev,gu} - \omega_\lambda - \omega_\kappa) - |t|\gamma_{eg}}. \tag{A9}$$

Next, we consider a model for potential surfaces of the electronic states g and e. Here we employ the displaced-distorted harmonic potential surfaces consisting of multi-modes. In this case, we notice that

$$\langle ev|gu\rangle = \prod_j \langle ev_j|gu_j\rangle, = \prod_j N_{ev_j} N_{gv_j} \int_{-\infty}^{\infty} dQ_j\, H_{ev_j}\left(\sqrt{\frac{\omega_j'}{\hbar}} Q_j'\right) H_{gu_j}\left(\sqrt{\frac{\omega_j}{\hbar}} Q_j\right) \times \exp\left[-\frac{\omega_j'}{2\hbar} Q_j'^2 - \frac{\omega_j}{2\hbar} Q_j^2 \right]. \tag{A10a}$$

$$\omega_{ev,gu} = \omega_{eg} + \sum_j \left[(v_j + 1/2)\omega_j' - (u_j + 1/2)\omega_j \right], \tag{A10b}$$

and

$$P_{gu} = \prod_i P_{gu_i} = \prod_i 2\sinh(\hbar\omega_i/kT) e^{-(u_i+1/2)\hbar\omega_i/kT} \tag{A10c}$$

where, for example,

$$N_{ev_j} = \sqrt{\frac{\sqrt{\beta'/\pi}}{2^{v_j} v_j!}}.$$

Substituting equations (A10) into (A9) and applying the Slater sum to the resulting expression lead to

$$W^{(2)}_{e\leftarrow g} = \frac{2\Delta_\lambda \Delta_\kappa}{\hbar^2}\left|S^{\vec{\lambda}\vec{\kappa}}_{eg}\right|^2 \alpha^T_{e\leftarrow g}(\omega_{eg}-\omega_\lambda-\omega_\kappa), \quad \text{(A11a)}$$

where

$$\alpha^T_{e\leftarrow g}(\omega_{egi}-\omega_\lambda-\omega_\kappa) = \frac{1}{2\pi}\int_{-\infty}^{\infty} dt\, e^{it(\omega_{eg}-\omega_\lambda-\omega_\kappa)-|t|\gamma_{eg}} G(t). \quad \text{(A11b)}$$

Here the nuclear correlation function $G(t)$ is given by [52]

$$G(t) = \prod_j G_j(t) \quad \text{(A12a)}$$

where

$$G_j(t) = \frac{2\sqrt{\omega_j\omega_j'}}{\omega_j+\omega_j'}\frac{1}{e^{it(\omega_j-\omega_j')}(1+n)-n} \times \frac{e^{it(\omega_j-\omega_j')/2}}{\sqrt{f_{j+}(t,n_j')f_{j-}(t,n_j')}}\exp\left[-\frac{\omega_j\omega_j'(\Delta Q_j)^2}{\hbar(\omega_j+\omega_j')}\frac{g_{j\mathrm{disp}}(t,n_j')}{f_{i+}(t,n_j')}\right], \quad \text{(A12b)}$$

In equation (A12), we used the following functions [45, 52]

$$f_{j\pm}(t,n_j') = 1 \pm \left(\frac{\omega_j-\omega_j'}{\omega_j+\omega_j'}\right) g_{i-}(t,n_j'), \quad \text{(A13a)}$$

$$g_{j\pm}(t,n_j') = (1+n_j')e^{it\omega_i'} \pm n_j' e^{-it\omega_i'}, \quad \text{(A13b)}$$

$$g_{j\mathrm{disp}}(t,n_j') = 1 + 2n_j' - g_{i+}(t,n_j'), \quad \text{(A13c)}$$

and

$$n_j' = \frac{1}{e^{it(\omega_j-\omega_j')+\hbar\omega_j/kT}-1}. \quad \text{(A13d)}$$

Polarization dependence

It is obvious from equation (A6) that one should take an average over orientations of molecules in equation (A11) for the case when various orientations can occur. The projection of the matrix element of the electronic dipole moment operator $\vec{\mu}_{e'g}$, which is expressed in the molecular coordinate system along the laboratory fixed direction of the polarization of light, is given by [22]

$$\vec{\lambda}\cdot\vec{\mu}_{e'g} = \sum_A \lambda_A \mu^A_{e'g}, \quad \text{(A14)}$$

where $A = (X, Y, Z)$. The electronic transition dipole moments $\mu^A_{e'g}$ are connected with $\mu^a_{e'g}$ expressed in terms of molecular fixed coordinates, via the transformation [22]

$$\mu^A_{e'g} = \sum_a \xi_{Aa}(\vec{\Omega})\mu^a_{e'g}, \quad \text{(A15)}$$

where $a = (x, y, z)$ represents molecular fixed coordinates, and $\vec{\Omega}$ stands for the Euler angles. Substituting equations. (A14) and (A15) into (A6) yields

$$S^{\vec{\lambda}\vec{\kappa}}_{eg} = \sum_A\sum_B\sum_a\sum_b \lambda_A\kappa_B\xi_{Aa}\xi_{Bb}S^{ba}_{eg}, \quad \text{(A16)}$$

where

$$S^{ba}_{eg} = \sum_{e'}\left[\frac{\mu^b_{ee'}\mu^a_{e'g}}{\omega_{e'g}-\omega_\kappa}+\frac{\mu^a_{ee'}\mu^b_{e'g}}{\omega_{e'g}-\omega_\lambda}\right]. \quad \text{(A17)}$$

To obtain an expression for the transition probability of randomly oriented non-rotating molecules, one should average $W^{(2)}_{e\leftarrow g}$ over all the molecular orientations,

$$\left\langle W^{(2)}_g\right\rangle = \sum_e\left\langle W^{(2)}_{e\leftarrow g}\right\rangle = \frac{2\Delta_\lambda\Delta_\kappa}{\hbar^2}\sum_A\sum_B\sum_C\sum_D\sum_a\sum_b\sum_c\sum_d\left\langle\lambda_A\kappa_B\lambda_C^*\kappa_D^*\xi_{Aa} \times\xi_{Bb}\xi_{Cc}\xi_{Dd}\right\rangle\sum_e S^{ba}_{eg}(S^{dc}_{eg})^*\alpha^T_{e\leftarrow g}(\omega_{eg}-\omega_\lambda-\omega_\kappa). \quad \text{(A18)}$$

According to Weyl's theorem [54], one finds that

$$\left\langle\lambda_A\kappa_B\lambda_C^*\kappa_D^*\xi_{Aa}\xi_{Bb}\xi_{Cc}\xi_{Dd}\right\rangle = \frac{1}{30}[\delta_{AB}\delta_{CD}(4\delta_{ab}\delta_{cd}-\delta_{ac}\delta_{bd}-\delta_{ad}\delta_{bc}) + \delta_{AC}\delta_{BD}(-\delta_{ab}\delta_{cd}+4\delta_{ac}\delta_{bd}-\delta_{ad}\delta_{bc}) + \delta_{AD}\delta_{CB}(-\delta_{ab}\delta_{cd}-\delta_{ac}\delta_{bd}+4\delta_{ad}\delta_{bc})]. \quad \text{(A19)}$$

It should be noted that equation (A19) completely separates the photon and molecular parts. In other words, one can take the summation in equation (A18) over the photon and molecular variables independently.

$$\left\langle W^{(2)}_{e\leftarrow g}\right\rangle = (\delta^T_F F + \delta^T_G G + \delta^T_H H), \quad \text{(A20)}$$

Table A1. Polarization variables.

	Case 1		Case 2	
Polarization variables	λ Z[a]	κ Z[a]	λ RC[b]	κ RC[b]
F	2		−2	
G	2		3	
H	2		3	

[a] Z refers to the Z-direction polarized light.
[b] RC refers to the right-circularly polarized light.

where

$$\delta_F^T = \frac{1}{15}\frac{\Delta_\lambda \Delta_\kappa}{\hbar^2}\sum_a\sum_b S_{eg}^{aa}(S_{eg}^{bb})^*\alpha_{e\leftarrow g}^T \times \left(\omega_{eg}-\omega_\lambda-\omega_\kappa\right) \quad \text{(A21a)}$$

$$\delta_G^T = \frac{1}{15}\frac{\Delta_\lambda \Delta_\kappa}{\hbar^2}\sum_a\sum_b S_{eg}^{ba}(S_{eg}^{ba})^*\alpha_{e\leftarrow g}^T \times \left(\omega_{eg}-\omega_\lambda-\omega_\kappa\right) \quad \text{(A21b)}$$

$$\delta_H^T = \frac{1}{15}\frac{\Delta_\lambda \Delta_\kappa}{\hbar^2}\sum_a\sum_b S_{eg}^{ba}(S_{eg}^{ab})^*\alpha_{e\leftarrow g}^T \times \left(\omega_{eg}-\omega_\lambda-\omega_\kappa\right) \quad \text{(A21c)}$$

$$F = 4\left|\vec{\lambda}\cdot\vec{\kappa}\right|^2 - 1 - \left|\vec{\lambda}\cdot\vec{\kappa}^*\right|^2 \quad \text{(A21d)}$$

$$G = -\left|\vec{\lambda}\cdot\vec{\kappa}\right|^2 + 4 - \left|\vec{\lambda}\cdot\vec{\kappa}^*\right|^2 \quad \text{(A21e)}$$

and

$$H = -\left|\vec{\lambda}\cdot\vec{\kappa}\right|^2 - 1 + 4\left|\vec{\lambda}\cdot\vec{\kappa}^*\right|^2. \quad \text{(A21f)}$$

Table A1 lists the values of F, G, and H for two particular cases.

It is instructive to illustrate the low temperature limit, i.e., $\hbar\omega_j/kT \gg 1$. In this case we find, for example,

$$\delta_F^{T=0} = \frac{1}{15}\frac{\Delta_\lambda \Delta_\kappa}{\hbar^2}\sum_a\sum_b S_{eg}^{aa}(S_{eg}^{bb})^*\alpha_{e\leftarrow g}^{T=0}\left(\omega_{eg}-\omega_\lambda-\omega_\kappa\right), \quad \text{(A22a)}$$

where

$$\alpha_{e\leftarrow g}^{T=0}(\omega_{eg}-\omega_\lambda-\omega_\kappa) = \frac{1}{2\pi}\int_{-\infty}^{\infty} dt\, e^{it(\omega_{eg}-\omega_\lambda-\omega_\kappa)-|t|\gamma_{eg}} \times \prod_j \frac{2\sqrt{\omega_j\omega_j'}}{\omega_j+\omega_j'}\frac{e^{-it(\omega_j-\omega_j')/2}}{\sqrt{f_{j+}(0)f_{j-}(0)}} \times \exp\left[-\frac{\omega_j\omega_j'(\Delta Q_j)^2}{\hbar(\omega_j+\omega_j')}\frac{g_{j\,\mathrm{disp}}(0)}{f_{j+}(0)}\right]. \quad \text{(A22b)}$$

We used equation (A22) for our numerical calculations.

References

[1] W.M. Jackson, D.S. Anex, R.E. Continetti, B.A. Balko, Y.T. Lee, *J. Chem. Phys.*, **95,** 7327 (1991).
[2] W. Sun, K. Yokoyama, J.C. Robinson, A.G. Suits, D.M. Neumark, *J. Chem. Phys.*, **110,** 4363 (1999).
[3] A.M. Mebel, W.M. Jackson, A.H.H. Chang, S.H. Lin, *J. Am. Chem. Soc.*, **120,** 5751 (1998).
[4] W.M. Jackson, A.M. Mebel, S.H. Lin, Y.T. Lee, *J. Phys. Chem.*, **101,** 6638 (1997).
[5] X. Song, Y. Bao, R.S. Urdahl, J.N. Gosine, W.M. Jackson, *Chem. Phys. Lett.*, **217,** 216 (1994).
[6] C.-K. Ni, J.-D. Huang, Y.-T. Chen, A.H. Kung, W.M. Jackson, *J. Chem. Phys.*, **110,** 3320 (1999).
[7] J.H. Kiefer, P.S. Mudipalli, S.S. Sidhu, R.D. Kern, B.S. Jursic, K. Xie, H. Chen, *J. Phys. Chem.* A, **101,** 4057 (1997).
[8] M. Yoshimine, J. Pacansky, N. Honjou, *J. Am. Chem. Soc.*, **111,** 4198 (1989).
[9] M. Yoshimine, J. Pacansky, N. Honjou, *J. Am. Chem. Soc.*, **111,** 2785 (1989).
[10] N. Honjou, J. Pacansky, M. Yoshimine, *J. Am. Chem. Soc.*, **107,** 5332 (1985).
[11] L.H. Sutcliffe, A.D. Walsh, *J. Chem. Phys.*, **19,** 1210 (1951).
[12] L.H. Sutcliffe, A.D. Walsh, *J. Chem. Soc. (London)*, 899 (1952).
[13] J.W. Rabalais, J.M. McDonald, V. Scherr, S.P. McGlynn, *Chem. Rev.*, **71,** 73 (1971); T. Shimanouchi, Tables of Molecular Vibrational Frequencies. Consolidated Vol. I, National Bureau of Standards, Washington (1972).
[14] A.A. Iverson, B.R. Russell, *Spectrochim. Acta* A, **28,** 447 (1972).
[15] O.A. Mosher, W.M. Flicker, A. Kuppermann, *J. Chem. Phys.*, **62,** 2600 (1975).
[16] K. Fuke, O. Schnepp, *Chem. Phys.*, **38,** 211 (1979).
[17] J. Diamond, G.A. Segal, *Chem. Soc.*, **106,** 952 (1984).
[18] A.M. Mebel, Y.-T. Chen, S.H. Lin, *Chem. Phys. Lett.*, **258,** 53 and references therein (1996).
[19] A.M. Mebel, Y.-T. Chen, S.H. Lin, *J. Chem. Phys.*, **105,** 9007 and references therein (1996).
[20] J.-L. Chang, G.-C. Tseng, C.-K. Ni, J.-D. Y.-T. Huang, Chen, *J. Phys. Chem.* A, **103,** 6063 (1999).
[21] J.-C. Shieh, J.-L. Chang, J.-C. Wu, R. Li, A.M. Mebel, N.C. Handy, Y.-T. Chen, *J. Chem. Phys.*, **112,** 7384 (2000).
[22] S.H. Lin, Y. Fujimura, H.J. Neusser, E.W. Schlag, *Multiphoton Spectroscopy of Molecules*, Academic, Orlando, FL, (1984).
[23] K. Chen, E.S. Yeung, *J. Chem. Phys.*, **69,** 43 (1978).
[24] J.-L. Chang, J.-C. Shieh, J.-C. Wu, R. Li, Y.-T. Chen, *Chem. Phys. Lett.*, **325,** 369 (2000).
[25] J.-L. Chang, R. Li, J.-C. Wu, J.-C. Shieh, Y.-T. Chen, *J. Chem. Phys.*, **115,** 5925 (2001).
[26] J.-C. Wu, R. Li, J.-L. Chang, Y.-T. Chen, *J. Chem. Phys.*, **113,** 7286 (2000).
[27] C.-W., Liang, C.-C. Chen, C.-Y. Wei, Y.-T. Chen, *J. Chem. Phys.*, **116,** 4162 (2002).
[28] C.-C. Chen, H.C. Wu, C.M. Tseng, Y.H. Yang, Y.-T. Chen, *J. Chem. Phys.*, **119,** 241 (2003).
[29] F.A. Hamprecht, A.J. Cohen, D.J. Tozer, N.C. Handy, *J. Chem. Phys.*, **109,** 6264 (1998).
[30] N.C. Handy, D.J. Tozer, *J. Comp. Chem.*, **20,** 106 (1999).
[31] D.J. Tozer, N.C. Handy, *J. Chem. Phys.*, **109,** 10 180 (1998).

[32] R. Bauernschmitt, M. Haser, O. Treutler, R. Ahlrichs, *Chem. Phys. Lett*., **264,** 573 (1997).
[33] C. Jamorski, M.E. Casida, D.R. Salahub, *J. Chem. Phys*., **104,** 5134 (1996).
[34] M. Petersilka, E.K.U. Gross, *Int. J. Quantum Chem. Symp*., **30,** 181 (1996).
[35] R. van Leeuwen, E. Baerends, *J. Phys. Rev*., **A49,** 2421 (1994).
[36] S.J.A. van Gisbergen, F. Kootstra, P.R.T. Schipper, O.V. Gritsenko, J.G. Snijders, E. Baerends, *J. Phys. Rev*., **A57,** 2556 (1998).
[37] R.D. Amos, I.L. Alberts, J.S. Andrews, S.M. Colwell, N.C. Handy, D. Jayatilaka, P.J. Knowles, R. Kobayashi, G.J. Laming, A.M. Lee, P.E. Maslen, C.W. Murray, P. Palmieri, J.E. Rice, E.D. Simandiras, A.J. Stone, M.-D. Su, D.J. Tozer, Cadpac 6.5. The Cambridge Analytic Derivatives Package (1998).
[38] (a) H.-J. Werner, P.J. Knowles, *J. Chem. Phys*., **82,** 5053 (1985); (b) P.J. Knowles, H.-J. Werner, *Chem. Phys. Lett*., **115,** 259 (1985).
[39] (a) H.-J. Werner, P.J. Knowles, *J. Chem. Phys*., **89,** 5803 (1988); (b) P.J. Knowles, H.-J. Werner, *Chem. Phys. Lett*., **145,** 514 (1988).
[40] MOLPRO is a package of *ab initio* programs written by H.-J. Werner, P.J. Knowles, with contributions from J. Almlöf, R.D. Amos, M.J.O. Deegan, S.T. Elbert, C. Hampel, W. Meyer, K. Peterson, R. Pitzer, A.J. Stone, P.R. Taylor, R. Lindh.
[41] K.B. Wiberg, C.M. Hadad, J.B. Foresman, W.A. Chupka, *J. Phys. Chem*., **96,** 10 756 (1992).
[42] P. Baltzer, B. Wannberg, M. Lundqvist, L. Karlsson, D.M.P. Holland, M.A. MacDonald, W. von Niessen, *Chem. Phys*., **196,** 551 (1995).
[43] A.M. Mebel, M. Hayashi, S.H. Lin, In *Trends in Physical Chemistry*, p. 315, Research Trends, India (1997).
[44] G. Herzberg, *Molecular Spectra and Molecular Structure* III, Van Nostrand-Reinhold, New York (1966).
[45] A.M. Mebel, M. Hayashi, K.K. Liang, S.H. Lin, *J. Phys. Chem*. A, **103,** 10 674 (1999).
[46] A.M. Mebel, Y.-T. Chen, S.H. Lin, *Chem. Phys. Lett*., **275,** 19 (1997).
[47] C.D. Pibel, A. Mcllroy, C.A. Taatjes, S. Alfred, K. Patrick, J.B. Halpern, *J. Chem. Phys*., **110,** 1841 (1999).
[48] J.-L. Chang, R. Li, J.-C. Wu, J.-C. Shieh, Y.-T. Chen, *J. Chem. Phys*., **115,** 5925 (2001).
[49] J.-L. Chang, Y.-T. Chen, *J. Chem. Phys*., **116,** 7518 (2002).
[50] D.-W. Liao, A.M. Mebel, Y.-T. Chen, S.H. Lin, *J. Phys. Chem*. A, **101,** 9925 (1997).
[51] D.-W. Liao, A.M. Mebel, M. Hayashi, Y.J. Shiu, Y.-T. Chen, S.H. Lin, *J. Chem. Phys*., **111,** 205 (1999).
[52] Y.J. Shiu, M. Hayashi, A.M. Mebel, Y.-T. Chen, S.H. Lin, *J. Chem. Phys*., **115,** 4080 (2001).
[53] C.-W. Liang, C.-C. Chen, C.-Y. Wei, Y.-T. Chen, *J. Chem. Phys*., **116,** 4162 (2002).
[54] D.P. Craig, T. Thiranamachandran, In *Molecular Quantum Electrodynamics*, p. 311, Academic Press, New York (1984).